

## Research



Article submitted to journal

**Subject Areas:**

astrophysics, computer modelling and simulation, wave motion

**Keywords:**

sun, atmosphere, waves, magnetohydrodynamics, internal gravity waves

**Author for correspondence:**

G. Vigeesh

e-mail: [vigeesh@leibniz-kis.de](mailto:vigeesh@leibniz-kis.de)

## On the influence of magnetic topology on the propagation of internal gravity waves in the solar atmosphere

G. Vigeesh<sup>1</sup>, M. Roth<sup>1</sup>, O. Steiner<sup>1,2</sup> and B. Fleck<sup>3</sup><sup>1</sup>Leibniz-Institut für Sonnenphysik (KIS), Schöneckstraße 6, 79104 Freiburg, Germany<sup>2</sup>Istituto Ricerche Solari Locarno (IRSOL), Via Patocchi 57, 6605 Locarno-Monti, Switzerland<sup>3</sup>ESA Science and Operations Department, c/o NASA/GSFC Code 671, Greenbelt, MD, USA

The solar surface is a continuous source of internal gravity waves (IGWs). IGWs are believed to supply the bulk of the wave energy for the lower solar atmosphere, but their existence and role for the energy balance of the upper layers is still unclear, largely due to the lack of knowledge about the influence of the Sun's magnetic fields on their propagation. In this work, we look at naturally excited IGWs in realistic models of the solar atmosphere and study the effect of different magnetic field topographies on their propagation. We carry out radiation-magnetohydrodynamic (R-MHD) simulations of a magnetic field free and two magnetic models – one with an initial, homogeneous, vertical field of 100 G magnetic flux density and one with an initial horizontal field of 100 G flux density. The propagation properties of IGWs are studied by examining the phase-difference and coherence spectra in the  $k_h$ - $\omega$  diagnostic diagram. We find that IGWs in the upper solar atmosphere show upward propagation in the model with predominantly horizontal field similar to the model without magnetic field. In contrast to that the model with predominantly vertical fields show downward propagation. This crucial difference in the propagation direction is also revealed in the difference in energy transported by waves for heights below 0.8 Mm. Higher up, the propagation properties show a peculiar behaviour, which require further study. Our analysis suggests that IGWs may play a significant role in the heating of the chromospheric layers of the internetwork region where horizontal fields are thought to be prevalent.

© The Author(s) Published by the Royal Society. All rights reserved.

## 1. Introduction

Waves are a ubiquitous phenomenon in the atmosphere of a star, including that of the Sun. Of the different types of waves present in the solar atmosphere, internal gravity waves (IGWs) are perhaps the least studied of them all. Propagating with frequencies below the acoustic waves, IGWs are buoyancy-driven waves naturally occurring in a continuously stratified fluid. The solar atmosphere happens to be an ideal environment for their generation, sustenance and eventual dissipation.

The main driver of IGWs in the solar atmosphere are the convective updrafts penetrating into the stably stratified atmospheric layer above. IGWs have been detected in the solar atmosphere and are thought to significantly contribute towards the total wave energy flux in the lower atmosphere [1]. Low-frequency ultraviolet (UV) brightness fluctuations observed in the internetwork region of the low solar chromosphere are believed to be caused by IGWs dissipating in the higher layers [2]. However, the strong effects of magnetic field orientation (attack angle) on the propagation of IGW have been demonstrated by Newington & Cally [7,8] and realistic numerical simulations have shown that the magnetic field present in the solar atmosphere influence the propagation of these waves and likely hinder them from propagating into the upper atmosphere [3–5]. At this point it is still unclear what role the magnetic field plays in the propagation of IGWs into higher layers and how this fits with the brightness fluctuations seen in chromosphere.

While it is well known that the quiet solar atmosphere is permeated by magnetic field, the exact topology of the magnetic field depends on whether one examines a network or an internetwork region on the solar surface. The network field is mainly characterised by strong vertical component that form magnetic flux concentrations which merge with other network field bundles outlining a supergranulation cell. The area surrounded by the supergranular network (i.e., the cell interior) is usually referred to as the internetwork, where the magnetic field topology is of more mixed orientation, often with a predominance of horizontal fields. The internetwork usually has fewer strong, vertical flux tubes and is mainly pervaded by weaker horizontal fields. For a recent review on the observational aspects of the quiet solar magnetism, the reader is referred to Bellot Rubio et al. [6].

What does this mean for IGWs propagating in a magnetic environment as diverse as the solar atmosphere? The combined effect of buoyancy, gas pressure, and magnetic field results in a more complicated picture of magneto-acoustic-gravity waves than the one simply described by the acoustic-gravity wave spectrum, wherein the waves are clearly decoupled throughout the atmosphere. The complexity arises due to the additional anisotropy introduced by the magnetic field direction, leading to a multitude of wave modes that depend locally on the angle between the direction of gravitational acceleration and the magnetic field. Furthermore, the highly dynamic and inhomogeneous atmosphere of the Sun provides an environment in which changes happen rapidly from region to region rendering it practically impossible to assign an average property to the atmosphere as seen by a passing wave. This is much more important for IGWs, as local changes may happen faster than the characteristic time scales of the waves.

The effect of magnetic field on the propagation of IGWs in a model solar atmosphere permeated by a uniform static magnetic field of different orientations were undertaken by Newington & Cally [7,8]. They showed that in regions of highly inclined magnetic fields, IGWs undergo mode conversion to upward propagating (field-guided) acoustic or Alfvénic waves. They suggest that the upward propagating acoustic waves are then likely to dissipate by shock formation before reaching the upper chromosphere, while converted Alfvénic waves can propagate to higher layers. In contrast to the case of highly inclined field, the presence of a vertical field results in the reflection of these waves back into the lower atmosphere. Radiative damping effects do not play a significant role in the mode conversion higher up, but may be important in the surface layers where the IGWs are likely generated.

In this paper, we address this problem with more realistic models of the solar magnetic environment that mimic the atmospheric conditions as closely as possible. Our aim is to better understand the link between the brightness fluctuations in the internetwork region and internal gravity waves, and the role of the magnetic field topology on their propagation characteristics. This paper extends on the previous studies [3–5] by comparing the propagation of IGWs in models with different magnetic field orientations. These environments are far from idealistic and have magnetic field properties that are more representative of the network/internetwork-like regions of the solar surface.

The outline of this paper is as follows: in §2 we present the models that we use in this study and describe the data analysis method for investigating waves, in §3 we present the results of our wave analysis and in §4 we provide our conclusions.

## 2. Method

We carry out full three-dimensional simulations of the near-surface layer of the Sun using the CO<sup>5</sup>BOLD code [9]. The numerical code solves the time-dependent nonlinear MHD equations in a 3D Cartesian domain with an external gravity field and including non-grey radiative transfer. Approximately, the lower half of the computational domain is in the convective layer and the upper half extends into the stable atmospheric layer where the waves we are interested in propagate. The waves are studied by looking at characteristic properties revealed by their dispersion relation. In the following, we describe the construction of the models and the data analysis in more detail.

### (a) Numerical models

We consider three models that mainly differ in the initial magnetic field introduced before the start of the simulation. Firstly, a non-magnetic model (Sun-v0) is constructed by setting the initial magnetic flux density to zero. In order to mimic a magnetic network-like environment, we construct a second model with an initial, vertical, homogeneous field of 100 G flux density (Sun-v100). Finally, to represent the magnetic field behaviour in an internetwork-like region, we build a third model with an initial, horizontal, homogeneous field of 100 G flux density (Sun-h100). The former two models were part of an earlier study [4,5]. In this work, we present the new model that is constructed by introducing a horizontal magnetic field aligned in the  $x$  coordinate direction. All models, including the field free model, were calculated with the very same MHD-solver (HLL-MHD; see Freytag et al. [9]). All three simulations are carried out on a computational domain of  $38.4 \times 38.4 \times 2.8 \text{ Mm}^3$ , discretized onto a  $480 \times 480 \times 120$  mesh. The domain extends  $\sim 1.3 \text{ Mm}$  above and  $\sim 1.5 \text{ Mm}$  below the mean Rosseland optical depth  $\tau_R=1$ . For more details on the numerical setup, the reader is referred to Vigeesh et al. [4].

The main difference between the three models is in the initial condition. Additionally, they also differ in the prescription of the top and bottom boundary conditions for the magnetic field. We use periodic boundary conditions for the side boundaries for all the three models. This dictates the fluid flow, radiation, and the magnetic field components to be periodic in the lateral direction. The top boundary is open for flow and radiation and the in-flowing material at the bottom boundary carries with it a constant specific entropy to maintain the radiative flux corresponding to an effective temperature ( $T_{\text{eff}}$ ) of  $\sim 5770 \text{ K}$ . For the vertical field model (Sun-v100), the top and bottom boundary condition is such that the vertical component of the magnetic field is constant across the boundary and the transverse component drops to zero at the boundary. For the horizontal field case (Sun-h100), the vertical component of the magnetic field is fixed at its initial value of zero and a constant extrapolation applies to the transverse component across the boundary. The bottom boundary condition for the Sun-v100 model is the same as its top boundary condition. For the Sun-h100 case, however, the up-flowing material carries with it horizontal magnetic flux density of 100 G when ascending into the computational domain.

The three set of simulations were run for 4 hr with a snapshot captured every 30 s, giving a total of 480 time points. Figure 1 shows the outward radiative flux, normalized by  $\sigma T_{\text{eff}}^4$ , as a function of time for the three simulations. It should be noted that this quantity is measured at a higher cadence. The vertical magnetic model (Sun-v100) shows a slightly elevated effective temperature presumably due to the radiative channeling effect of vertical flux concentration [10]. Independent of the different initial and boundary conditions, all models show a stable radiative output throughout the entire span of the simulation run. Having such a similar, stable and continuous time series allows us to perform Fourier analysis for studying waves and comparing them on an equal footing.

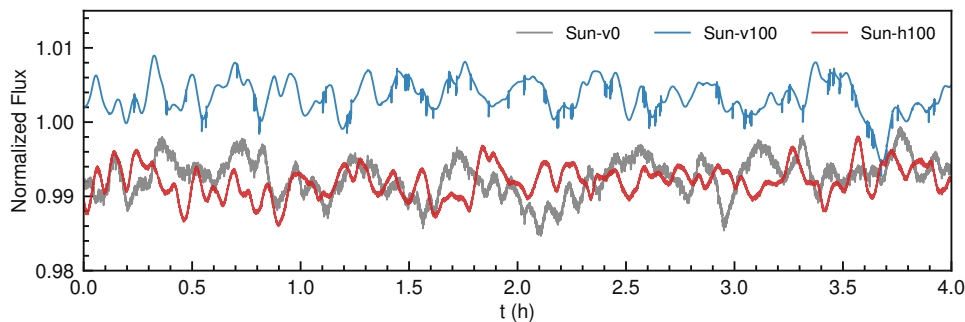


**Figure 1.** Outward radiative flux, normalized by  $\sigma T_{\text{eff}}^4$ , as a function of time for the non-magnetic (Sun-v0) in gray, vertical (Sun-v100) in blue, and horizontal field (Sun-h100) model in red.

Figure 2 shows the temperature at a reference level of  $\tau_R = 1$  and the absolute magnetic field strength at the same layer, for snapshots taken 3 hours after the start of the simulation for each of the three models. The granular structure, represented here in grayscale, is similar in all the models. The total magnetic field strength is overplotted on the two magnetic models: Sun-v100 (center) and Sun-h100 (right). We note from these maps that most of the magnetic flux in the Sun-v100 is preferentially located in the intergranular lanes, while the Sun-h100 model does not harbor as much vertical flux concentrations as the former case. The magnetic field in the Sun-h100 case is more scattered and shows mixed orientations at the  $\tau_R = 1$  reference layer.

The difference in topology of the magnetic models in both cases can be seen by examining a vertical section through the computational domain. In Figure 3 we show a representation of the magnetic field lines on a  $x$ - $z$  plane in a small region of the Sun-v100 (top panel) and Sun-h100 (bottom panel) models. The region is arbitrarily chosen to show a fully developed magnetic flux concentration in both of the models. Also shown overlaid on the plots are the contours of  $\tau_R=1$  in white and the plasma- $\beta=1$  in red, where plasma- $\beta$  is the ratio of the gas pressure to magnetic pressure. The difference between the two models can be clearly discerned from the magnetic field orientation. The main difference occurs above the equipartition surface  $\beta=1$  layer, where for the Sun-v100 model we have predominantly vertical field components and for the Sun-h100 model the field lines are predominately horizontal with vertical footpoints connecting them to the intergranular lane. The plasma- $\beta$  contour in these two examples is shown to dip below the  $\tau_R=1$  contour with the magnetic field strength surpassing 1 kG at these locations. Between the height where the average  $\tau_R=1$  and average plasma- $\beta=1$ , the two models are similar and show mixed orientation of the magnetic field but with a preference to their initial direction, except of course at the locations of flux concentration where they are vertically aligned.

In Figure 4, the left panel shows the ratio of mean absolute vertical component of the magnetic field ( $|B_z|$ ) to the absolute field strength  $|\mathbf{B}|$  of both models and the right panel shows the area fraction covered by  $|\mathbf{B}| > 1$  kG field of both models as a function of height. In the case of Sun-v100, for layers above  $z = 0$  Mm, we see that a fraction of more than 0.75 of the magnetic flux

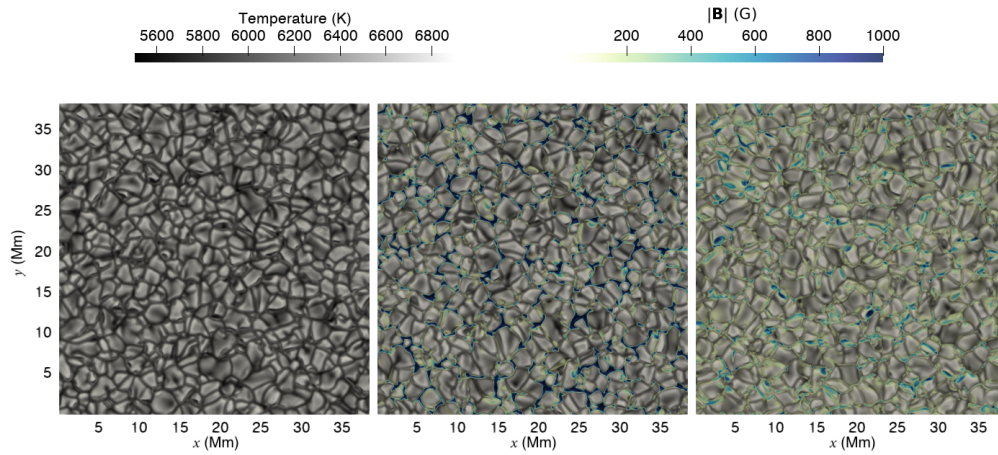


**Figure 2.** Temperature at a reference level of  $\tau_R = 1$  (in gray) and absolute magnetic field strength at  $\tau_R = 1$  (in color with  $\alpha$ -blending to highlight the stronger fields) from the three models of solar magnetoconvection: Sun-v0 (left), Sun-v100 (middle), and Sun-h100 (right). The snapshots shown here are taken 3 hr after the start of the simulation.

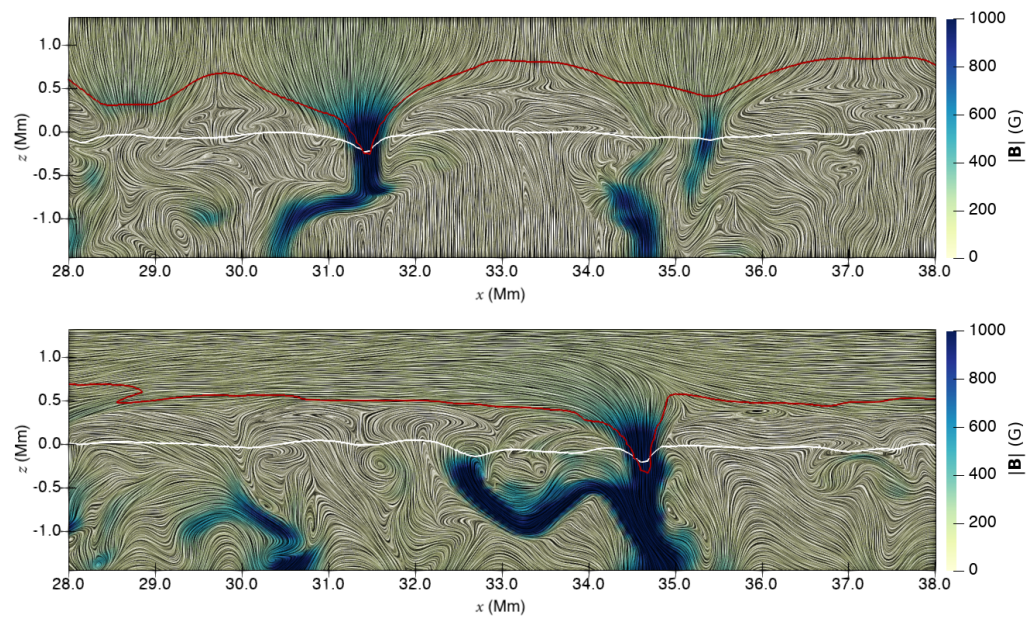


**Figure 3.** Visualization of magnetic fields (colored) in the  $x$ - $z$  plane showing the predominant orientation of the field in the two magnetic simulations: Sun-v100 (top) and Sun-h100 (bottom). The white contours denote the  $\tau_R = 1$  surface and the red contour is the plasma- $\beta = 1$  surface.

density is vertically directed and increases with height above  $z = 0.5$  Mm reaching 100% at the top boundary due to the boundary condition. The area fraction that is covered with  $|\mathbf{B}| > 1$  kG in the Sun-v100 model is 0.1–0.2 in the range  $z = 0$  to 0.5 Mm, decreasing with height further above. The initial increase is the result of the fanning of magnetic flux concentrations in the lower part of the atmosphere. In the case of Sun-h100, only less than 40% of the magnetic flux density is vertically directed in the lower solar atmosphere, decreasing with height to 0% at the top boundary as a

result of the boundary condition. The area fraction that is covered with  $|\mathbf{B}| > 1$  kG in the Sun-h100 model is less than 0.06.

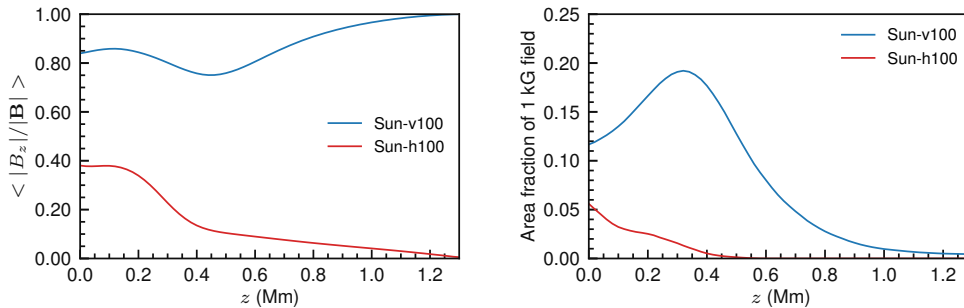


**Figure 4.** Ratio of mean absolute vertical component of magnetic field ( $B_z$ ) to the total mean  $\mathbf{B}$  (left panel) and the area fraction covered by  $|\mathbf{B}| > 1$  kG field (right panel) in the Sun-v100 (blue) and Sun-h100 (red) models as a function of height.

Measurement of the quiet Sun magnetic fields is particularly difficult in the upper solar atmosphere. Indirect methods using spectropolarimetric data reveal a prevalence of horizontal fields in the internetwork region [14], with loop like structures protruding from the surface [13]. These loops show a “flattened” geometry as they rise through the temperature minimum region. We believe that the internetwork region is pervaded with such loops and in the vicinity of the temperature minimum region they might tend to have a predominantly horizontal field topology due to their “flattened” nature. The network region on the other hand can be thought of as being dominated by the footpoints of the low-lying loops as well as long reaching vertical flux concentrations, thereby giving them a predominantly vertical field topology.

### (b) Wave diagnostics

After a sufficient duration of the simulation is complete, 4 hrs in our case, we extract different physical quantities from the simulation to perform a spectral analysis. The spectral analysis is carried out by decomposing the physical quantities into their Fourier components in the horizontal direction and in time for each grid level in the  $z$ -direction. The Fourier synthesis is performed using the fast Fourier transform (FFT) algorithm, and the components are then represented on a  $k_h$ - $\omega$  dispersion relation diagram for a given height by azimuthally averaging over the  $k_x$ - $k_y$  plane. The phase difference and coherence spectra of the velocities at two separate layers are then computed from the complex cross-spectrum,  $S_{v_1, v_2}(\mathbf{k}, \omega) = v_1(\mathbf{k}, \omega) \cdot \overline{v_2(\mathbf{k}, \omega)}$ , where  $v_1$  represents the velocity at layer 1 and likewise for  $v_2$ , and the overbar represents the complex conjugate (see Eqs. 4-6 of Vigeesh et al. [3]). The confidence interval for the phase and coherence measurements and the zero coherence threshold are also computed as described in Vigeesh et al. [5]. To study the energy transport by these waves, we estimate the mechanical energy flux spectra by computing the perturbed pressure-velocity ( $\Delta p - v$ ) co-spectrum represented on the  $k_h$ - $\omega$  dispersion relation diagram.

## 3. Results

In this section, we present the results from our wave analysis that show the differences in wave propagation between the three models introduced in §2(a). We then discuss about the similarities and differences in energy transport by IGWs in the different models. Lastly, we briefly mention the effect of the background flow on the dissipation of these waves.

## (a) Wave generation and propagation

We study the propagation characteristic of the waves by examining the velocity-velocity ( $v-v$ ) phase difference spectra represented in the  $k_h-\omega$  diagnostic diagram for a given pair of heights. Observed  $k_h-\omega$  phase diagrams usually result from time series of simultaneously acquired Dopplergrams in a number of spectral lines, formed at different heights. For the simulation, we can extract the velocity field for any pair of atmospheric layers and compute the phase-difference spectra between those. In Figure 5, we show the phase difference between the vertical velocity measured at  $z = 100$  km and  $z = 120$  km of the three models, represented on the  $k_h-\omega$  diagnostic diagram. This near surface region where the waves are presumably excited show similar IGW emission characteristics – downward phase propagation (negative phase difference) in the region below the IGW propagation boundary (marked by the lower black solid and dashed curves). The corresponding energy transport is upward directed, indicating that these waves are indeed IGWs. In the rest of the paper, we refer with “upward” or “downward” propagation to the direction of energy transport, which for gravity waves is opposite to the direction of phase propagation. An upwardly propagating gravity wave has downwardly propagating phase and shows up with a negative phase difference according to our sign convention when calculating phase difference spectra (phase of lower layer minus phase of upper layer).

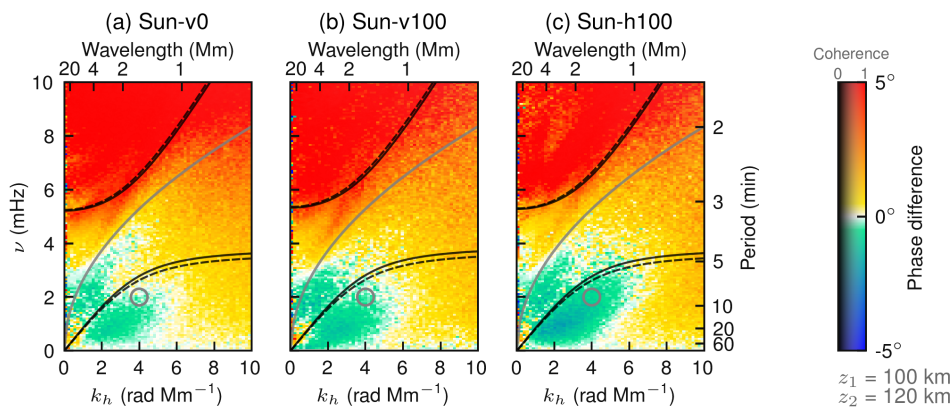


**Figure 5.**  $v_z - v_z$  phase and coherence spectra estimated between  $z = 100$  km and  $z = 120$  km for the (a) non-magnetic model, Sun-v0, (b) model with predominantly vertical fields, Sun-v100, and (c) model with the predominantly horizontal fields, Sun-h100. The dashed black curves represent the propagation boundaries for the lower height, and the solid curves represent those for the upper height. The gray curve represents the dispersion relation of the surface gravity waves. The colors represent the phase difference and the shading shows the coherence. IGWs propagate in the region below the lower propagation boundaries.

Although the near surface region show similar wave spectra, higher up in the atmosphere the three models show markedly different behaviour on the  $k_h-\omega$  phase difference spectra for a given pair of heights. Rather than limiting ourselves to a single pair of heights, we look at how the phase difference and coherence vary as a function of vertical distance between the measurement heights in the three models. Figure 6 shows the phase difference and coherence as a function of travel distance relative to a reference height of  $z=0$  Mm (thick curves) for the non-magnetic (grey: Sun-v0), the vertical field model (blue: Sun-v100), and the horizontal field model (red: Sun-h100). This is computed by estimating the  $v_z-v_z$  phase difference and coherence between  $z=0$  Mm and every grid point along the  $z$ -direction. The plots correspond to a given Fourier component, here  $k_h \approx 4$  rad Mm $^{-1}$  and  $\nu \approx 2$  mHz, which fall in the region of the  $k_h-\omega$  where the bulk of the IGWs occur in our simulation (location marked by the circle in Fig 5). The 90% confidence bounds for the phase difference and coherence estimates are shown by the shaded areas and the zero-coherence

threshold is shown by the dashed-grey line. We also show the phase difference and coherence relative to a selection of other reference layers, viz.  $z = 0.4, 0.6, 0.8$  Mm. These plots clearly reveal the difference in the propagation properties of waves in models without, with vertical, and with horizontal magnetic fields.

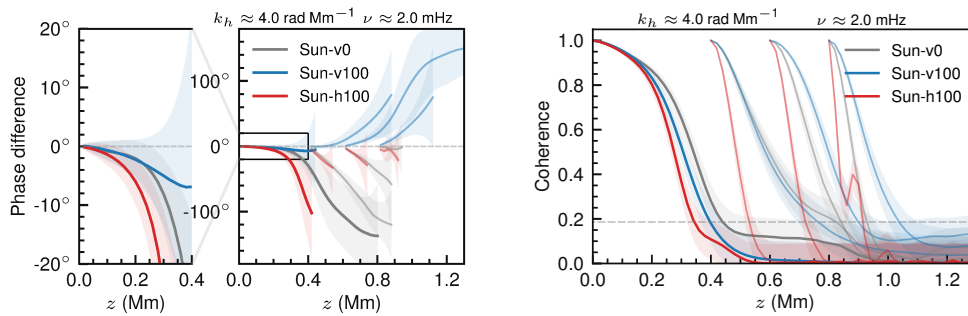


**Figure 6.**  $v$ - $v$  phase difference (left) and coherence (right) between the reference layer,  $z = 0$  Mm, and layers of constant geometrical scale for a given  $k_h$  and  $\omega$  (thick curves) for the three models. The leftmost subplot is a rescaled part of the small region in the panel, marked by a black rectangle. The thin solid lines show three other reference layers. The 90% confidence bounds for estimates are represented by the shaded area. The zero-coherence threshold at a significance level of 0.05 is marked by the dashed line in the right plot.

Firstly, all the three models show negative phase difference up to around 0.4 Mm, suggesting that the waves in these model propagate in the upward direction (downward propagating phase). We note here that beyond the travel distance of 0.4 Mm for the  $z = 0$  Mm reference layer, the phase difference measurements in both the magnetic models become unreliable as indicated by the break in the phase-difference spectra and by the uncertainty in the measurement shown by the shaded area. The coherence in all the three models above a height of 0.4 Mm drops below the zero-coherence threshold.

Particularly interesting to note is the difference in the phase and coherence spectrum for the reference layer of  $z = 0.4$  Mm and the same above. Here, we see that the non-magnetic model always shows negative phase-difference, suggesting that the waves are upward propagating throughout the atmosphere. However, when comparing the two magnetic models, we clearly see the influence of magnetic field orientation on the propagation of the IGWs. The model with a predominantly horizontal field reveals a similar behaviour as the non-magnetic case, showing negative phase-difference throughout the atmosphere, meaning that the IGWs propagate upwards as if the magnetic fields were absent. For the model with a predominantly vertical field, on the other hand, this is not the case as the phase difference here is positive for heights above  $z = 0.4$  Mm, revealing quite a contrasting behaviour compared to the non-magnetic and the model with horizontal field. The IGWs in the vertical field case are seen to propagate downwards in the higher layers.

The change in behaviour around  $z = 0.4$  Mm can be understood by looking again at Figure 3. We see here that the magnetic fields in the two models are quite similar in regions between the average  $\tau_R = 1$  surface and average  $\beta = 1$  surface which is around  $z = 0.5$  Mm. We believe that the similarity in both simulations in terms of wave propagation is due to the fact that the dynamics of the waves below the plasma  $\beta=1$  surface is not dominated by the magnetic fields, but by the thermodynamic properties of the atmosphere. The thermal properties of the atmosphere in the near surface layers are similar in the two cases of Sun-v100 and Sun-h100. In the low plasma  $\beta$  layers, however, the waves see a different magnetic field orientation between the two magnetic models as they propagate. This is an indication of the mode coupling that occurs in the presence of magnetic fields of different inclination as described by Newington & Cally [7,8].



## (b) Energy transport

The difference in the wave propagation behavior as revealed by the phase and coherence analysis presented in the previous section highlights an important aspect of the energy transport of these waves in the solar atmosphere.

In order to better understand the energy transport of the waves in the different models, we look at the mechanical energy flux computed in the  $k_h$ - $\omega$  diagnostic diagram for a given layer. In Figure 7, we show the mechanical flux as a function of height for the three models. Here, we show it for the same Fourier component ( $k_h \approx 4 \text{ rad Mm}^{-1}$ ,  $\nu \approx 2 \text{ mHz}$ ) as for the phase/coherence analysis above. In addition, for comparison we also show the fluxes for a Fourier component that correspond to the high-frequency acoustic wave ( $k_h \approx 4 \text{ rad Mm}^{-1}$ ,  $\nu \approx 8 \text{ mHz}$ ).

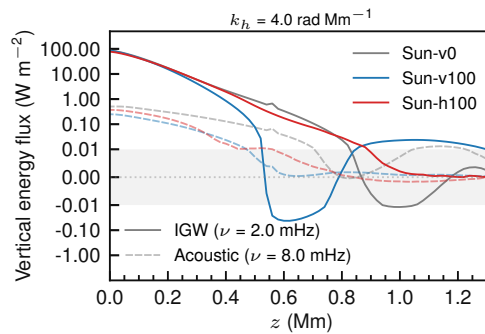


**Figure 7.** Mechanical flux as a function of height for a given  $k_h$  and  $\omega$  for the different models.

We see that for all the three models, the mechanical energy flux is upward directed up to a height of  $z \approx 0.5 \text{ Mm}$ , confirming the propagation properties that are revealed by the phase-difference analysis. Above this height, we see that the non-magnetic model and the model with horizontal field show a very similar behaviour exhibiting upward energy transport up to a height of  $\sim 0.9 \text{ Mm}$ , beyond which they tend to deviate. The reason for this behaviour is unclear. Nevertheless, the plot of the energy flux as a function of height suggests that the IGWs in a predominantly horizontal field environment may transport energy to higher layers, up to a height of  $\sim 0.9 \text{ Mm}$ . On the other hand, the model with vertical magnetic field shows a completely different behaviour above  $z = 0.5 \text{ Mm}$ . Here, we see that the energy transport is downward directed, which is what we expected from the phase-difference analysis. This suggests a markedly different energy transport behaviour of the IGWs in the presence of vertical magnetic field compared to a non-magnetic atmosphere or an atmosphere with a predominantly horizontal field. But here again, the behaviour around  $z = 0.8 \text{ Mm}$  and above remains unclear. We refrain from interpreting the results in the vicinity of the upper boundary ( $\sim 2$ - $3$  pressure scale heights), i.e. above  $z = 1 \text{ Mm}$  in the atmosphere where the coherence value drops below the zero-coherence threshold at 95% level anyway.

The peculiar behaviour above the height of  $z = 0.8 \text{ Mm}$  in all the three models suggests that this might have a different origin than the magnetic field itself. The measured phase difference and the energy transport for the chosen Fourier component do not fit the behaviour of IGW above  $z = 0.8 \text{ Mm}$ , the basic signature of which is the opposite sign of the vertical component of the phase propagation and energy transport. We do not have an explanation for this behavior and these waves might not be IGWs anymore. This is particularly surprising for the Sun-v0 case, because the selected Fourier component falls in the IGW range and should satisfy the acoustic-gravity dispersion relation. The boundary condition seems to have an influence only in the grid cells very close to the boundary. Perhaps a linear analysis breaks down due to the large amplitude of the thermodynamic perturbations in these layers. The temperature perturbations in the upper atmosphere is particularly strong for the Sun-v0 case. Exploring this aspect is extremely

important, but is beyond the scope of this work. A cause for the puzzling behaviour above the  $z = 0.8$  Mm level might be non-linear effects as is addressed in the following section.

### (c) Wave-breaking

When waves propagate in the presence of a background flow, their propagation properties are modified. Strong background flow may result in nonlinear breaking of IGWs, leading to enhanced energy dissipation. In the context of IGWs in the solar atmosphere, [11] considered a stability condition given by the ratio of wave vorticity ( $\zeta$ ) and the Brunt-Väisälä frequency,  $N$ , defined as,

$$N^2 = g \left( \frac{1}{H_\rho} - \frac{1}{\gamma H_p} \right), \quad (3.1)$$

where,  $\gamma$  is the ratio of the specific heats ( $c_P/c_V$ ),  $H_\rho$  is the density scale height, and  $H_p$  is the pressure scale height of the atmosphere.

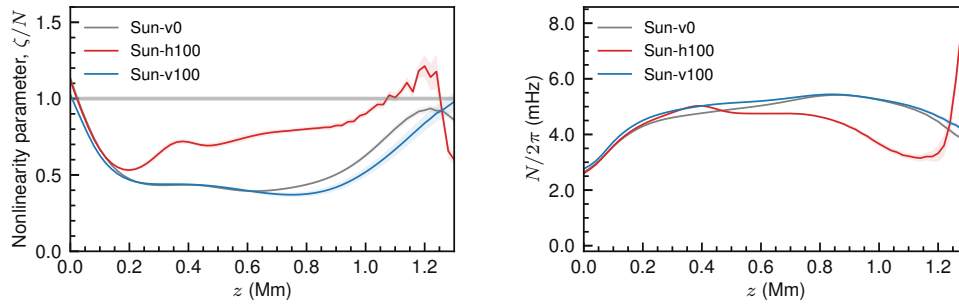


**Figure 8.** Nonlinearity parameter ( $\zeta/N$ , left panel) and the Brunt-Väisälä frequency ( $N$ , right panel) as a function of height in the three models. The peculiarities apparent in the Sun-h100 model above  $z \approx 1.2$  Mm are due to the influence of the upper boundary condition.

A non-zero vorticity may occur due to vortex flows or as a result of velocity shear. Here we consider the average fluid vorticity ( $\nabla \times \mathbf{v}$ ) as a proxy for the wave vorticity ( $\zeta$ ) to estimate the strength of the background flow [12]. In Figure 8, the left shows the ratio,  $\zeta/N$  and the right panel shows the Brunt-Väisälä frequency as a function of height for the three models. We see that for most of the atmosphere,  $\zeta/N$  is below unity, suggesting that the model does not have strong background flows to influence the propagation of IGWs. However, the horizontal field model seems to have a larger  $\zeta/N$  at higher layers compared to both the vertical field and non-magnetic case, suggesting that IGWs are more likely to break in the former case. The Sun-h100 model shows a lower Brunt-Väisälä frequency compared to the other models, as a result of the higher density and pressure scale height. A more detailed analysis would require estimating the wave vorticity in the  $k_h$ - $\omega$  diagnostic diagram and exploring the ratio for a given Fourier component, which is planned for the future. However, from the energy transport perspective, we have seen that horizontal magnetic field allow IGWs to propagate upwards into the atmosphere. Combined with the fact that, horizontal models also show stronger non-linearity parameter, this suggests that wave breaking may be a possible scenario by which IGWs dissipate their energy in an atmosphere with predominantly horizontal fields. Vertical fields, on the other hand, appear to prohibit IGWs from propagating into higher layers and therefore prevents them from undergoing wave-breaking at chromospheric heights.

The numerical solver used in this work is capable of capturing strong discontinuities related to wave breaking condition, but the coarse resolution of the simulation restricts us from exploring this aspect adequately. The models presented in this work are of low resolution ( $\delta x, \delta y = 80$  km)

that do not capture strong vorticity, and therefore it is unclear if wave breaking is still the reason for the decrease in energy flux that we observe. We see that the average temperature remains similar in the three models. Therefore, we cannot claim to have clear evidence of wave breaking or the consequent temperature enhancement in our simulation. High resolution simulations show significantly stronger flows and vorticity [12,15,16] and therefore maybe better suited for the study of wave breaking.

## 4. Conclusion

The complex and highly dynamic atmosphere of the Sun harbours internal gravity waves. They have been detected in observations and have been clearly reproduced in realistic three-dimensional numerical simulations of the solar atmosphere. In this work, we show that the energy flux spectra in the lower photosphere are dominated by upward propagating IGWs and are independent of the magnetic properties of the model. In the higher layers of the atmosphere, the average magnetic field orientation dictates the propagation properties of the IGWs. In vertical field models the IGWs are reflected downwards, whereas in models without a magnetic field and a horizontal magnetic field they propagate freely into the upper layers. Our study demonstrates that IGWs behave similarly in the near surface layers of internetwork-like region where the fields are predominantly horizontal and in network regions where the fields are predominantly vertical. In these low layers, the magnetic field does not play a significant role. However, the significant differences in behaviour between the two models in the upper layers above  $\approx 0.4$  Mm, demonstrate the importance of the orientation of the magnetic field for the propagation of IGWs. The upward propagation of IGWs in internetwork-like regions may lead to wave-breaking and therefore may be related to the brightness fluctuations seen in UV passbands. This is in agreement with the interpretation of the observed UV brightness fluctuations as signature of IGWs by Rutten et al. [2]. On the other hand, where there are predominantly vertical field components, like in network-regions, IGWs tend to reflect back without reaching wave-breaking heights and therefore may play only a minor role for the heating of the upper layers. The peculiar behaviour of the waves above  $z = 0.8$  Mm in our simulation is not understood and requires further study. A detailed comparison with observations should shed further light on the differences in wave propagation behaviour between internetwork and network regions.

**Data Accessibility.** The data this study is based on are too large to host on public repositories. However, parts of the data can be requested from the corresponding author, who will be happy to discuss ways to access the data.

**Authors' Contributions.** GV designed and carried out the simulations, performed the data analysis and drafted the manuscript. All authors read and contributed to the discussion and helped polish the manuscript.

**Competing Interests.** The author(s) declare that they have no competing interests.

**Funding.** This work was supported by the *Deutsche Forschungsgemeinschaft*, DFG grant RO 3010/3-1.

**Acknowledgements.** We thank the anonymous referee for exceptionally detailed and constructive comments, which helped to significantly improve the paper.

## References

1. Straus T, Fleck B, Jefferies SM, Cauzzi G, McIntosh SW, Reardon K, Severino G, Steffen M. 2008 The Energy Flux of Internal Gravity Waves in the Lower Solar Atmosphere. *Astrophys. J.* **681**, L125. [2008ApJ...681L.125S]
2. Rutten RJ, Krijger JM. 2003 Dynamics of the solar chromosphere IV. Evidence for atmospheric gravity waves from TRACE. *Astron. Astrophys.* **407**, 735–740. [2003A&A...407..735R]
3. Vigeesh G, Jackiewicz J, Steiner O. 2017 Internal Gravity Waves in the Magnetized Solar Atmosphere. I. Magnetic Field Effects. *Astrophys. J.* **835**, 148. [2017ApJ...835..148V]

4. Vigeesh G, Roth M, Steiner O, Jackiewicz J. 2019 Internal Gravity Waves in the Magnetized Solar Atmosphere. II. Energy Transport. *Astrophys. J.* **872**, 166. [[2019ApJ...872..166V](#)]
5. Vigeesh G, Roth M. 2020 Synthetic observations of internal gravity waves in the solar atmosphere. *Astron. Astrophys.* **633**, A140. [[2020A&A...633A.140V](#)]
6. Bellot Rubio L, Orozco Suárez D. 2019 Quiet Sun magnetic fields: an observational view. *Living Reviews in Solar Physics* **16**, 1. [[2019LRSP...16....1B](#)]
7. Newington ME, Cally PS. 2010 Reflection and conversion of magnetogravity waves in the solar chromosphere: windows to the upper atmosphere. *Mon. Not. R. Astron. Soc.* **402**, 386–394. [[2010MNRAS.402..386N](#)]
8. Newington ME, Cally PS. 2011 Mode conversion of radiatively damped magnetogravity waves in the solar chromosphere. *Mon. Not. R. Astron. Soc.* **417**, 1162–1169. [[2011MNRAS.417.1162N](#)]
9. Freytag B, Steffen M, Ludwig HG, Wedemeyer-Böhm S, Schaffenberger W, Steiner O. 2012 Simulations of stellar convection with CO5BOLD. *Journal of Computational Physics* **231**, 919–959. [[2012JCoPh.231..919F](#)]
10. Salhab RG, Steiner O, Berdyugina SV, Freytag B, Rajaguru SP, Steffen M. 2018 Simulation of the small-scale magnetism in main-sequence stellar atmospheres. *Astron. Astrophys.* **614**, A78. [[2018A&A...614A..78S](#)]
11. Mihalas BW, Toomre J. 1981 Internal gravity waves in the solar atmosphere. I - Adiabatic waves in the chromosphere. *Astrophys. J.* **249**, 349–371. [[1981ApJ...249..349M](#)]
12. Vigeesh G, Steiner O, Calvo F, Roth M. 2017 On the effect of vorticity on the propagation of internal gravity waves. *Mem. Soc. Astron. Ital.* **88**, 54. [[2017MmSAI..88...54V](#)]
13. Martínez González MJ, Manso Sainz R, Asensio Ramos A, Bellot Rubio LR. 2010 Small Magnetic Loops Connecting the Quiet Surface and the Hot Outer Atmosphere of the Sun. *Astrophys. J. Lett.* **714**, L94–L97. [[2010ApJ...714L..94M](#)]
14. Lites BW, Kubo M, Socas-Navarro H, Berger T, Frank Z, Shine R, Tarbell T, Title A, Ichimoto K, Katsukawa Y, Tsuneta S, Suematsu Y, Shimizu T, Nagata S. 2008 The Horizontal Magnetic Flux of the Quiet-Sun Internetwork as Observed with the Hinode Spectro-Polarimeter. *Astrophys. J.* **672**, 1237–1253. [[2008ApJ...672.1237L](#)]
15. Fleck B, Carlsson M, Khomenko E, Rempel M, Steiner O, Vigeesh G. 2020 Acoustic-gravity wave propagation characteristics in 3D radiation hydrodynamic simulations of the solar atmosphere. *arXiv e-prints* arXiv:2007.05847. [[2020arXiv200705847F](#)]
16. Canivete Cuissa JR, Steiner O. 2020 Vortices evolution in the solar atmosphere. A dynamical equation for the swirling strength. *Astron. Astrophys.* **639**, A118. [[2020A&A...639A.118C](#)]